applied sciences

MDPI

Article

Active Thermography for the Detection of Sub-Surface Defects on a Curved and Coated GFRP-Structure

Friederike Jensen *, Marina Terlau, Michael Sorg and Andreas Fischer

Institute for Metrology, Automation and Quality Science, University of Bremen, 28329 Bremen, Germany; m.terlau@bimaq.de (M.T.); m.sorg@bimaq.de (M.S.); andreas.fischer@bimaq.de (A.F.)
* Correspondence: f.jensen@bimaq.de

Abstract: Initial defects, for example, those occurring during the production of a rotor blade, encourage early damages such as rain erosion at the leading edge of wind turbine rotor blades. To investigate the potential that initial defects have for early damage, long-pulse thermography as a non-destructive and contactless measurement technique is applied to a strongly curved and coated test specimen for the first time. This specimen is similar in structural size and design to a rotor blade leading edge and introduced with sub-surface defects whose diameters range between 2 mm and 3.5 mm at depths between 1.5 mm and 2.5 mm below the surface. On the curved and coated test specimen, sub-surface defects with a depth-to-diameter ratio of up to 1.04 are successfully detected. In particular, defects are also detectable when being observed from a non-perpendicular viewing angle, where the intensity of the defects decreases with increasing viewing angle due to the strong surface curvature. In conclusion, long-pulse thermography is suitable for the detection of sub-surface defects on coated and curved components and is therefore a promising technique for the on-site application during inspection of rotor blade leading edges.

Keywords: active thermography; sub-surface defects; defect visualization; automatic defect detection; leading edge; wind turbine rotor blade; coated and curved surface; GFRP-structure

Citation: Jensen, F.; Terlau, M.; Sorg, M.; Fischer, A. Active Thermography for the Detection of Sub-Surface Defects on a Curved and Coated GFRP-Structure. *Appl. Sci.* **2021**, *11*, 9545. https://doi.org/10.3390/app11209545

Academic Editors: Xavier Maldague, Valérie Kaftandjian-Doudet, Ahmad Osman, Bastien Chapuis, Gunther Steenackers and Hai Zhang

Received: 15 September 2021
Accepted: 9 October 2021
Published: 14 October 2021

1. Introduction

The rotor blade leading edge of a wind turbine is heavily loaded by the high rotational speed (over 300 km/h at the blade tip) and the environmental mechanical influences such as rain, wind or dust. The resulting damage due to erosion leads to an increase in surface roughness at the leading edge, which changes the aerodynamic properties of the rotor blade negatively [1]. Such partial surface damages lead to premature transitions of the boundary layer flow from laminar to turbulent [2], which has a significant influence on the degree of efficiency of the wind turbine [3] and thus leads to losses of the annual energy production [4]. The repair of a rotor blade leading edge with severe damage is expensive and complicated and the quality of the repair is strongly dependent on the experience of the technicians. Furthermore, poorly executed repairs bring new susceptibility to erosion during operation. Therefore, various solutions to protect the leading edge have been developed, such as coatings, leading edge tapes and erosion shields (erosion shields are currently not used because an attachment solution is missing [5]). Nevertheless, erosion damage still occurs. Regular monitoring and early maintenance of the rotor blade is therefore recommended.

The rotor blade itself consists of two half-shells glued together and supported by central thrust webs. The half-shells are made of a glass fiber-reinforced plastic (GFRP) strengthened by a sandwich structure of foam or balsa. Carbon fiber-reinforced plastic (CFRP) chords in the center of the rotor blade and ribs in the rear blade area provide increased stiffness. The rotor blade is coated with a polyurethane-based coating system. The first few millimeters of the leading edge material thus consist of the coating system and

GFRP laminate. Studies indicate that initial sub-surface defects, such as voids, delaminations and low resin content in the GFRP, voids or foreign particles in the coating system and at the boundary layer between coating (or tape) and GFRP are responsible for premature erosion [6,7]. Voids occur, for example, as a result of air infiltration during the production of GFRP laminates, when the coating or the leading edge tape is applied. Foreign particles, e.g., dust, that become trapped in the coating during its application are also production defects [8]. Since material defects are stress raisers that can provoke rotor blade damages, they need to be investigated in detail. The very first step is to enable the detection of sub-surface material defects, which then allows to study the defects' potential to result in premature erosion damage as well as to study the damage progression under rain loading. Therefore, a non-destructive measuring technique is required, which enables the contactless detection of near-surface defects in coated and curved GFRP and is applicable on rotor blades of wind turbines even in the open field.

To examine a rotor blade leading edge regarding production and material defects, a non-destructive and contactless measurement technique is required that can detect blade defects in the near-surface area within or underneath a coating. These defects include voids, delaminations, inclusion of foreign particles or low resin content. They range in lateral size from around 1 m for delaminations to a few millimeters or even micrometers for voids or trapped dust particles, although the effect of the defect size on the later damage development is not yet clear.. Furthermore, the measuring technique should have imaging capabilities to enable the fast investigation of the entire leading edge in as few sections as possible. Several different non-destructive measuring techniques for the investigation and monitoring of wind turbine blades exist, such as acoustic emission measurements, guided waves, ultrasonic testing, strain measurements, thermographic measurements, radiography testing or visual inspection [9]. Indeed, visual inspection is the standard maintenance method, but sub-surface defects remain hidden. Some of the other methods require a variety of sensors to be mounted on the rotor blade and are therefore contact-based. Other measurement methods are time-consuming, only suitable for conductive material or have a complex measurement setup [10]. In the recent years, however, thermography has been proven to be a useful non-destructive measuring technique method for the inspection of rotor blades. Thermography works without contact, offers a simple measuring setup, has sufficient imaging capabilities (fast image acquisition of large areas) and the provided image results in the form of thermograms can be directly interpreted during inspection [11]. Furthermore, it enables the detection of sub-surface defects [10], which include production and material defects.

In active thermography, the test specimen is first heated by an energy source and in the subsequent cooling phase, the differences in the temperature distribution on the surface of the test specimen are recorded with an infrared camera and visually displayed in a thermogram [12]. Different active thermography methods like pulse, step-heating and long-pulse thermography have been developed, which differ in their excitation and recording routine. In pulse thermography, the sample is excited for a few milliseconds (mostly 2 ms to 10 ms) with a flash lamp at high power. The thermograms are recorded during the cooling phase. In contrast, long-pulse and step-heating thermography principles excite the sample for several seconds (ranging from 5 s to 300 s and more) using halogen lamps at lower power. In long-pulse thermography, the recording takes place during the cooling phase while in step-heating thermography the thermograms are already recorded during the excitation in the warm-up phase [13]. These different active thermography methods have been used in various investigations to obtain defect detection for rotor blades of wind turbines.

To evaluate the thermographic detectability of defects, the depth-to-diameter ratio is used [14]. It results from the depth at which the defect is located below the surface divided by the corresponding defect diameter. Due to the lateral heat transfer that takes place in the material between the surface and the defect, a defect with a depth-to-diameter ratio of ≥ 1 is considered to be barely detectable. In most experimental investigations, flat

and uncoated reference objects (GFRP and CFRP) modified with flat bottom holes were studied [15–18] to reduce unfavourable influences on the results due to a curved geometry or a coated surface. Kaminska et al., for example, carried out investigations on a GFRP plate modified with flat bottom holes [19]. Both pulse thermography and step-heating thermography were applied. In the case of step-heating thermography, the cooling phase was also considered in addition to the warm-up phase, which corresponds to the principle of long-pulse thermography. By comparing the different types of excitation, it was found that pulse thermography is particularly well suited for the investigation of near-surface defects while step-heating thermography emphasizes deeper defects. The results of the raw data of both thermographic methods show that defects with a diameter of 4 mm in a depth of 2 mm could be detected, which equals a depth-to-diameter ratio of 0.5. As long-pulse thermography has a higher sensitivity for defects in low thermal conductivity and low thermal response rate materials (such as GFRP) than pulse thermography, long-pulse thermography is preferred for the detection of deeper-lying defects [20]. In addition to the investigations on flat plates, there are also approaches for the thermographic investigation of curved surfaces. Wei et al. used pulse thermography to investigate impact damage on a curved CFRP specimen that was exposed to both thermal loads and ballistic impacts [21]. Both principal component analysis (PCA) and specially trained neural networks were able to detect the damage. Da Silva et al. also carried out investigations on a curved CFRP specimen modified with flat bottom holes using step-heating thermography [22]. In the cooling phase, inserted defects with a depth-to-diameter ratio of 0.25 could be detected. Curved GFRP specimens with an inner radius of 92 mm were investigated by Pastuszak et al. [23]. Using long-pulse thermography, delaminations in the form of teflon strips inserted into the laminate as well as the effect of static loads on the specimen were mapped experimentally and in simulations. Although the tests were performed on curved specimens, the used specimens did not possess a coating nor a strong enough curvature to be able to make comparisons with a real rotor blade leading edge in the tip section.

To extract the information that is contained in the raw thermograms efficiently, signal processing algorithms are applied. The most common advanced post-processing methods are thermographic signal reconstruction, PCA, absolute thermal contrast and phase Fourier analysis [24,25]. These data processing methods reduce thermal image artefacts, which are caused by non-uniform heating or thermal reflections from the environment. In this way, the detectability of defects is increased and a quantification is possible [26]. Sanati et al., for example, performed a comparison of pulse and step-heating thermography on a coated GFRP sample. They concluded that the collected data during both phases (warm-up and cooling) of step-heating thermography with a subsequent evaluation of the phase images (generated by Fourier transformation) gave the best results [27]. Defects larger than 4 mm could be detected in a depth of up to 2 mm, which is a depth-to-diameter ratio of 0.5. Wang et al. made a quantitative comparison of phase, step-heating, and long-pulse thermography [18]. For this purpose, they likewise modified a GFRP plate with flat drilled holes of 10 mm to 2.5 mm diameter, which were located between 0.5 mm and 3 mm below the surface to be excited. Phase image analysis as well as a PCA for all excitation methods were used for the data evaluation. The results of long-pulse thermography in combination with a PCA revealed most defects. Thus, defects with a diameter of 5 mm at a depth of 2 mm and defects with a diameter of 2.5 mm at a depth of 1.5 mm were detected, which results in a depth-to-diameter ratio of 0.4 and 0.6, respectively. Wei et al. have achieved similar results by the combination of long-pulse thermography and PCA on a GFRP plate modified with flat bottom holes [16]. Panella et al. performed a case study on a GFRP plate modified with various flat bottom holes by using long-pulse thermography with halogen lamps as excitation [15]. Different heating times between 5 s and 40 s were applied to the test specimen. With the use of PCA, defects with a depth-to-diameter ratio of 0.825 (depth = 6.6 mm, diameter = 8 mm) could be detected. Phase Fourier analysis as well as PCA are widely used and are established image processing methods that extract the desired information from thermograms and have therefore been used in various research papers.

While PCA uses general orthogonal functions, which provide a sparse representation of the thermographic data, phase Fourier analysis works on the basis of harmonic functions. Since in long-pulse thermography the sample is excited with only one light pulse, oscillatory signals in the thermographic data are less pronounced, which is why the application of PCA is more obvious here.

To assess the signal quality, the signal-to-noise ratio (SNR) is a typically used figure of merit. The higher the SNR, the better the signal is distinguished from background noise. For the quantification of the defect detectability in thermograms, a modified version of the SNR is often used, in which the contrast between two regions of the image (e.g., defect-affected area and defect-free/surrounding area) is defined as a signal and related to the surrounding noise [15,17]. In order to evaluate the distinguish ability of two areas similar to the SNR, the contrast-to-noise ratio (CNR) is a commonly used quantity [28,29]. Since the contrast between a defect and its surroundings is key for the defect detection, the calculation of the CNR to assess the image quality concerning a subsequent defect detection is preferred here.

Despite the variety of research work already conducted in the field of active thermography on rotor blades and on GFRP components, no experiments have been carried out on the leading edge of the rotor blades so far. Mostly flat GFRP panels, which are predominantly uncoated, have been investigated. Investigations on curved GFRP specimens are rare and have only been performed on specimens with relatively large radiation, which tend to be found in the root region of rotor blades rather than in the tip area, where the most intense load exist. Therefore, the existing findings are only transferable to a limited extent to the examination of a coated leading edge of a wind turbine rotor blade. In particular, investigations of test samples with a coating and with a defect diameter of less than 4 mm are necessary in order to gain insights into the influence of initial defects on the premature occurrence of erosion. In addition, the resolvable depth-to-diameter ratio as well as the achievable CNR for coated and strongly curved GFRP test specimens need to be clarified.

The aim of this work is to introduce active thermography for the special application of examining a rotor blade leading edge regarding initial production defects and material defects. In order to investigate the detectability of different defects, coated test specimens with a strong curvature, which correspond in shape, material, and structure to a rotor blade leading edge tip section of a real wind turbine, are modified with drillings in the lower single-digit millimeter range to imitate small hidden voids in the material. For the examination of the test specimen, long-pulse thermography in combination with a PCA is used. In Section 2, the measuring principle of long-pulse thermography as well as the image evaluation approach are described in detail. The description of the test specimens and the experimental test set-up including the test procedure follows in Section 3. Section 4 deals with the presentation of the experimental results and their discussion, while the important findings and conclusions are summarized together with an outlook in Section 5.

2. Materials and Methods

2.1. Long-Pulse Thermography

For the examination of the coated and curved test specimen, long-pulse thermography in reflected mode is used, where the excitation unit and the infrared camera are located on the same side of the test specimen. The schematic representation is shown in Figure 1.

The sample is excited optically for several seconds, which induces a heat flow in the sample. In homogeneous materials the heat propagation is uniform. If there are inhomogeneities such as air inclusions in the material, the heat flow is influenced by the different thermodynamic material properties. Thus, the reflected heat of the sample changes as well. When the heating phase and thus the excitation period is over, the cooling phase with the recording of the measurement data begins [13]. The local temperature differences on the surface of the test specimen during the cooling phase, which are caused by the material-dependent heat flow, are detected by an infrared camera and displayed

as a thermogram. The measured raw data are therefore the recorded radiation intensity images in the infrared range over time.

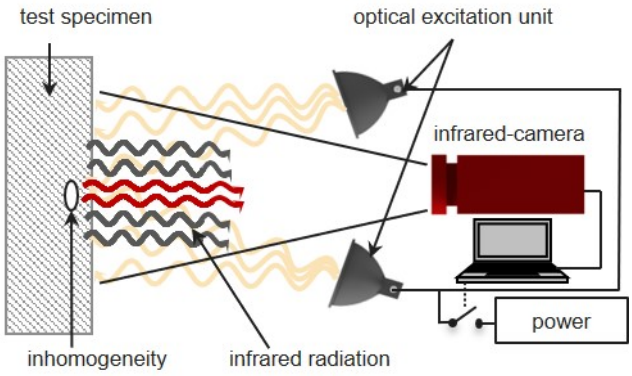

Figure 1. Schematic representation of long-pulse thermography in reflection mode.

In contrast to pulse thermography, long-pulse thermography is more suitable for low thermal response materials, since the long excitation time allows sufficient heat to penetrate into deeper layers of the load-bearing material. Furthermore, the heat sources are inexpensive and available in a large variety. In contrast to lock-in thermography, long-pulse thermography is faster because only one heating impulse is used, while lock-in thermography uses multiple short to long impulses. Wang et al. did comparative investigations between pulse thermography, step-heating thermography and long-pulse thermography combined with different classical evaluation methods such as PCA, phase Fourier analysis and thermographic signal reconstruction which showed that the best results for the investigation of fiber-reinforced materials were achieved with long-pulse thermography [18]. A disadvantage compared to pulse thermography or step-heating thermography, however, is the comparatively slow generation of data due to the long excitation recording time, which both are determined by the material's conductivity.

2.2. Signal Processing Methods

For the evaluation of the thermographic data two typical signal processing methods were used: principal component analysis and contrast-to-noise ratio. In order to increase the detectivity of material inhomogeneities and to extract the desired information from the thermal three-dimensional raw data, PCA is adapted from Rajic [30,31]. This method uses singular value decomposition to extract contrast information from the spatial and temporal information of the captured image sequence (3D matrix), which can then be visualized as an image. The singular value decomposition is represented as the product of three matrices:

$$A = USV^T \quad (1)$$

Here S is a diagonal matrix, which contains the singular values of the matrix A in the main diagonal. The columns of the matrix U consist of empirical orthogonal functions, which represent the spatial variations of the thermal data set, called spatial functions. The transposed matrix V^T describes the connection between the orthogonal functions [18]. When observing the cooling phase, the second spatial function is non-uniform and emphasizes areas of contrast [18,24]. Therefore, the second spatial function is utilized throughout the analysis to make inhomogeneities in the material visible.

To evaluate the visibility of potential defects, the contrast that exists between a defect and its surroundings is essential. To be able to compare the visibility of defects between

different images, the contrast is related to the surrounding noise. The so-called contrast-to-noise ratio (CNR) is calculated from the absolute contrast

$$C_{a,\mathrm{A-B}} = |\hat{I}_\mathrm{A} - \hat{I}_\mathrm{B}| \tag{2}$$

between the areas A and B of the pre-processed data and the corresponding standard deviation $S_{\mathrm{A-B}} = \sqrt{{S_\mathrm{A}}^2 + {S_\mathrm{B}}^2}$:

$$\mathrm{CNR} = \frac{|\hat{I}_\mathrm{A} - \hat{I}_\mathrm{B}|}{\sqrt{{S_\mathrm{A}}^2 + {S_\mathrm{B}}^2}}. \tag{3}$$

The absolute contrast $C_{a,\mathrm{A-B}}$ is calculated from the difference of the mean intensity values $\hat{I}_\mathrm{A}$ and $\hat{I}_\mathrm{B}$ of two areas A and B [28,29].

3. Experimental Set-Up

3.1. Measurement Object

For the sake of similarity to a real rotor blade leading edge of a wind turbine, the test specimen to be examined is accordingly adapted with respect to the geometry and the structural design. The left picture in Figure 2 shows the schematic structure of the test specimen. It consists of a hand-laminated GFRP half pipe with a length of 230 mm and an inner radius of $r_\mathrm{i} = 11$ mm. The specimen has a GFRP wall thickness of $s_\mathrm{GFRP} = 3.25$ mm. It consists of 4 layers of fiberglass laminate in biaxial $\pm 45°$ and unidirectional arrangement, with 815 g/m^2 per layer, and epoxy resin is used as matrix resin. While wind turbine rotor blades are often built with more layers of the composite material and thicker wall layers, the test specimen's materials are identical with those of real rotor blades. The coating system of the test specimen consists of a filler and a gel coating, both consisting of polyurethane. The filler and the coating are applied to the GFRP and have a combined thickness of approximately 0.5 mm. This coating system is applied in exactly the same way as in real rotor blades, so that the entire test specimen has a similar thermographic behaviour as the leading edge of a wind turbine rotor blade. The outer radius of the specimen including the coating system is 14.75 mm. For comparison, a typical blade profile of wind turbines, such as the NACA 4415 or the NACA 23015 [32], at a chord length of 1 m in the middle of the blade has a leading edge radius of about 25 mm. A chord length of 0.5 m at the tip region of the blade (where the load is the highest) the leading edge has a radius of about 12 mm [33]. Therefore, the present specimen radius is found in the outer third of the rotor blade towards the tip area.

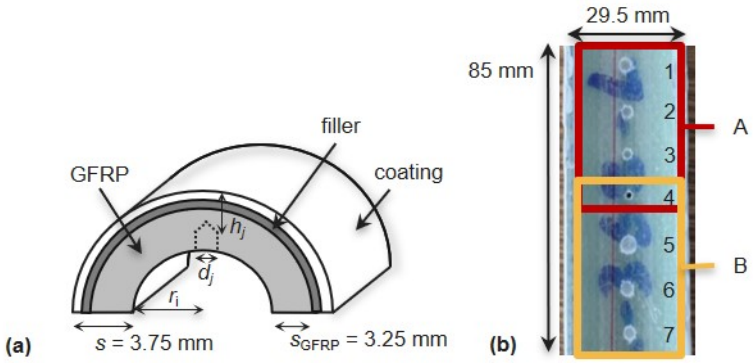

Figure 2. (**a**) schematic representation of the test specimen structure, (**b**) photograph of the rear side of the test specimen with seven drillings to imitate voids in the GFRP.

To imitate initial defects, the specimen is prepared with different drillings. In this case, voids are imitated by the application of standard drillings with a tapered tip, because it

closely matches the shape of trapped air bubbles near the surface. The drillings are placed at the rear side of the half pipe, so that when viewed from the front side, the drillings are at different depths h_j below the surface. This type of specimen preparation is easy to implement, allows reproducible tests and is used as standard method, in this case for the first time on curved and coated specimens. The right image in Figure 2 shows the rear side of the sample, divided into two regions of interest (ROI) A and B. Drillings 1 to 3 are approximately 1.5 mm below the surface and have a diameter of $d_1 = 3$ mm, $d_2 = 2.5$ mm and $d_3 = 2$ mm, respectively. Drillings 5 to 7 are located approximately 2.5 mm below the surface and have diameters of $d_5 = 3.5$ mm, $d_6 = 3$ mm and $d_7 = 2.5$ mm. This results in depth-to-diameter ratios between 0.5 and 1.04; see Table 1. Drilling 4 is a through-hole and serves as a marker for a better orientation in the thermograms.

Table 1. Properties of each defect of the modified test specimen in the two ROIs A and B, compare with Figure 2.

No.	ROI	Depth h_j [mm]	Diameter d_j [mm]	Depth-to-Diameter Ratio
1	A	1.5	3	0.50
2	A	1.4	2.5	0.56
3	A	1.5	2	0.75
4	A & B	0	1.5	-
5	B	2.4	3.5	0.69
6	B	2.2	3	0.73
7	B	2.6	2.5	1.04

3.2. Measurement System

For the execution of the test series a test set-up was developed, which is shown in Figure 3. It allows a flexible arrangement of the test sample, the excitation unit and the camera. A clamping device adapted to the sample geometry can be moved in horizontal and vertical direction via linear axes. A rotation motor enables a rotational adjustment of the sample. The excitation unit can be swivelled as well as placed on the base plate of the test facility. The camera can also be flexibly positioned on the base plate and its height can be adjusted. For the experiments performed in this paper a 1 kW halogen lamp in reflection mode (excitation and camera are on the same side of the sample) is used as excitation unit. The infrared camera is the Image IR 8300 from the company InfraTec with an image format of (640×512) px^2, a temperature resolution of 0.025 K and a spectral range of 2 µm to 5 µm. The chosen objective is a 100 mm telephoto objective in combination with a 500 mm close-up (macro) objective, which has an image field of (48×39) mm^2 with a spatial resolution of 75 µm. The distance between the camera lens and the test specimen is 500 mm.

For the investigations, two ROIs A and B are defined on the test specimen; see Figure 2. ROI A lies above the marking hole 4 of the test specimen, the region of interest B lies below the marker. Two test series are performed, one for each ROI. In every test series, various excitation times are investigated, each for different distances k between the sample and the excitation unit. For example, in test series 1, which deals with the ROI A, the test specimen is heated for $t_{\mathrm{exc}} = 10, 15, 20, 25$ and 30 s. For each excitation time, the distances $k = 22, 43, 60, 89, 114, 155$ and 300 mm are investigated. The infrared camera starts recording at 3 s after the end of the excitation and is done for at least 30 s with a frequency of 20 Hz and an integration time of 1600 µs. The test specimen is investigated from the front perspective as well as from two angular perspectives. The observation from two different angles of view α and β serves to examine the influence of the surface curvature on the defect visibility; see Figure 4. Table 2 shows an overview of the test series.

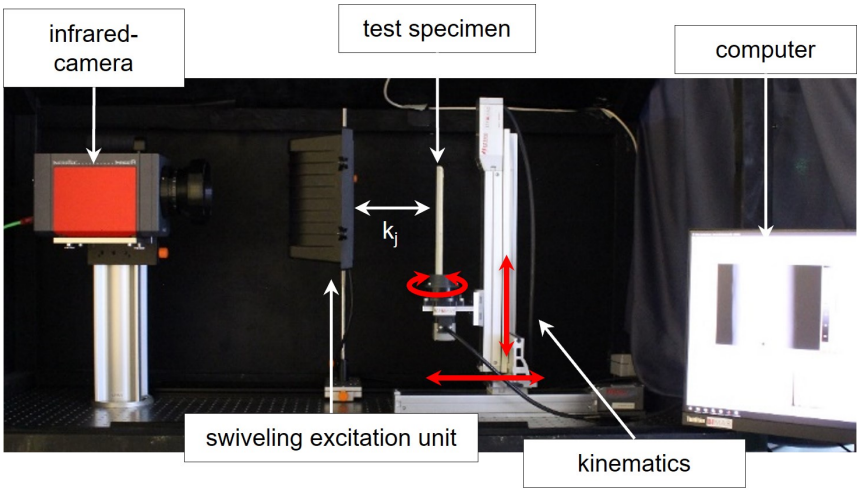

Figure 3. Photograph of the developed test set-up with the distance $k = 114$ mm between the excitation unit and the test specimen.

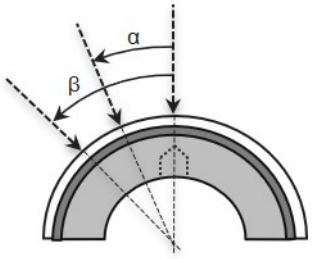

Figure 4. Schematic representation of the angular perspective with different offsets between the defect and the optical axis of the camera, $\alpha = 25°$ and $\beta = 45°$.

Table 2. Overview of the parameters of every test series, compared with the measurement arrangements shown in Figures 3 and 4.

Test Series	**1**	**2**	**3**
ROI	A	B	A
excitation time t_{exc} [s]	10, 15, 20, 25, 30	15, 20, 25, 30, 35	25
distance k [mm]	22, 43, 60, 89, 114, 155, 300		60
angular perspective α, β [°]	0		25, 45
excitation power [kW]	1		
recording time t_{rec} [s]	30		
rec. frequency [Hz]	20		
integration time [µs]	1600		

3.3. Image Processing

In the next step, an image processing, which is implemented in Python, is applied to the acquired thermogram sequences to extract the contrast information for the defect visualization as well as to detect the defects; see Figure 5. For the image processing, the first 15 s (300 thermograms) of the total recording are used, since the largest temperature gradients are found at the beginning of the cooling phase. Furthermore, only the ROIs shown in Figure 2 are considered in order to reduce artefacts and edge effects as well as to keep the computational effort and the processing time low. Furthermore, each image is normalized for the purpose of comparability. The largest intensity value of the image is assigned to the value 1, the smallest intensity value of the image is assigned to the value 0.

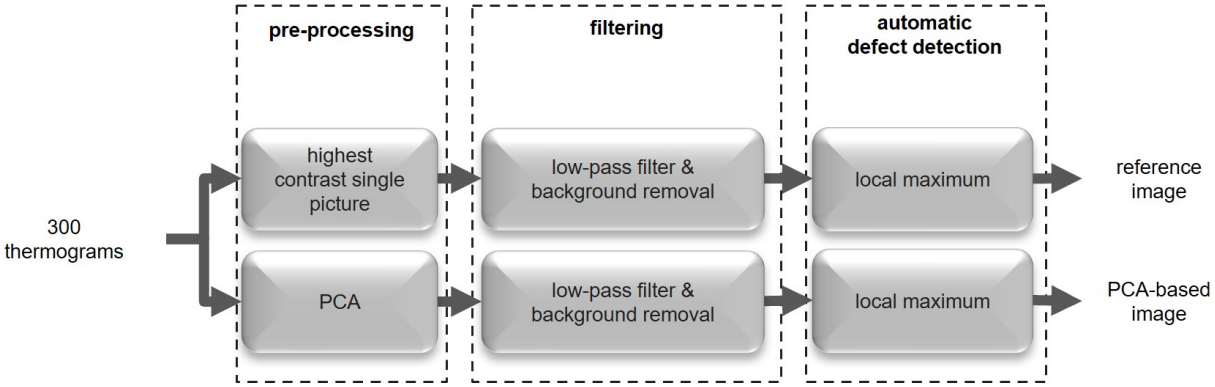

Figure 5. Signal flow diagram of the image processing operations.

As pre-processing methods, both the selection of the highest contrast single picture or a PCA are available. The algorithm for the highest contrast single picture selects one thermogram from the 300 thermograms that has the largest intensity difference between a defective and a non-defective area and thus the highest contrast. Mostly, the highest contrast is found in one of the first 10 pictures of the recording series, where the temperature at the defective area is significantly higher than at the non-defective area. With PCA, the output image is extracted from all thermograms; see Section 2.2. Here, the highest contrast single picture serves as a reference method to demonstrate the benefit of the PCA concerning information extraction and contrast enhancement.

For the filtering of the image and thus contrast enhancement, the noise in the resulting images of the pre-processing must be reduced. Therefore the images are filtered two times with a 16th order binomial filter acting as a low-pass filter. An additional contrast enhancement is achieved by removing the background. In this process, the minima located on a line between the defects, represented as image maxima, are found at first. Assuming that these minima correspond approximately to the image background, a threshold is set and the minima that lie beneath the threshold are eliminated. By interpolating between the different remaining image minima, a synthetic background is generated and subtracted from the image to be processed. To smoothen the resulting image, the same filter as before is applied again one time. This completes the filtering of the image.

In a final step, automatic defect detection is applied. Here, the detection algorithm searches for image maxima located at the same pixel of both an image column and an image row. These maxima are now detected as potential defects (feature extraction) and highlighted with a red circle. In order to clarify the contrast enhancement of the PCA and to be able to make quantitative statements about the defect visibility, the CNR of each potential defect in all resulting images (with and without filtering) is calculated; see Section 2.2. Assuming that the contrast distribution at and around a defect is normally distributed, the radius of the red circle results from the 3σ interval. Currently, the CNR threshold for the marking is set manually.

4. Results and Discussion

In the following section, the results of the different test series are presented and discussed. First, the general detectability of the sub-surface defects on curved and coated specimens is covered, based on test series 1 and 2. Then, the influence of the excitation time on the defect detection is investigated. Finally, based on test series 3, the influence of eccentric defects on the detectability is addressed.

4.1. Detectability of Sub-Surface Defects in Front Perspective

At first, test series 1 and 2 were carried out to see if defects beneath a coated surface can be detected by means of long-pulse thermography from a front perspective. Figure 6 shows the results of the first series of measurements at an excitation time of $t_{exc} = 15\,s$ and a distance $k = 89\,mm$ between excitation unit and test specimen. Figure 6a shows the first

thermogram recorded by the infrared camera, i.e., at $t_{rec} = 0$ s as an example. Most of the specimen, except its edges, stands out from its surroundings due to a higher temperature. Since the heating is inhomogeneous due to the curvature of the specimen and at the same time the emissivity of the specimen is dependent on the angle, the edges of the specimen appear cooler than the background. In the x-direction, the specimen has a thermal profile typical for the specimen's curvature: the center of the specimen is warmest because it is closest to the excitation, while the temperature decreases towards the edges. The defects inserted from behind in the form of drilled holes are already visible in the raw image due to local temperature variations on the surface of the test specimen. They stand out from their surroundings as bright spots due to their higher temperature. The emerging defects do not have a sharp boundary to their surroundings. Mainly the lateral heat flow due to spatially inhomogeneous heating, but also the specimen's material (heat propagation in fiber direction) and curvature as well as the defect shape (conical defects that become larger with increasing depth, see Table 1) as well as the defect depth affect the appearance of the defects in the image of the surface temperature distribution. Figure 6b shows the result of the highest contrast single picture pre-processing method (reference method) without filtering. The defects are notable as in the raw thermogram in Figure 6a. Figure 6c shows the highest contrast single picture pre-processed image with filtering, automatic defect detection and calculated CNR (reference image with filtering). All defects are detected in each of the investigated parameter combinations of this image processing path in test series 1. It is noticeable that the value of the CNR decreases from defect 1 to defect 3. Since all defects are located at the same depth about 1.5 mm below the surface, the difference in CNR is due to the different diameters of the defects. Defect 1 with the largest diameter accordingly has the largest CNR value. This correlates with the depth-to-diameter ratio, and the smaller the depth-to-diameter ratio is, the better the defect is detected. The largest depth-to-diameter ratio in ROI A has defect 3 with a value of 0.75, which is in the range of the maximal reported ratios in the current research. To increase the contrast of the image series, PCA is applied; see Figure 6d. As a result, not only do the defect areas stand out more clearly, but also the fiber structure of the upper GFRP layer of the test specimen is additionally revealed.

Figure 6e shows the PCA-based image with filtering, automatic defect detection and calculated CNR. The effect of PCA can be seen in the sharp increase in CNR values, e.g., from 189 to 2519 for defect 1. As for the reference image, the CNR values decrease as the depth-to-diameter ratio of each defect increases.

While the increase in contrast might be less relevant for test series 1, since all defects are already detectable in the reference image without filtering, the contrast increase is more important in test series 2. Figure 7 shows the results of the second test series with an excitation time of $t_{\mathrm{exc}} = 25$ s and a distance $k = 89$ mm between excitation unit and test specimen. In Figure 7a, as well as in the ROI B in Figure 7b, the typical temperature distribution for a curved surface can be seen, as in the previous test series. In contrast to ROI A, however, a very homogeneous temperature distribution can be seen in the center of the specimen. Defects 5 to 7, which are located below the surface, do not distinguish themselves by a local temperature maximum. Even by image filtering in Figure 7c, only defect 6 is detected. Note also that false detections occur during the evaluation, due to the local temperature distribution on the surface of the specimen in the defect area no longer being distinguishable from the temperature distribution of the surrounding area. On the one hand the defects are located deeper in the material and on the other hand, the material is inhomogeneous and natural accumulations of resin could be detected as defect incorrectly. Thus, artefacts caused by cross-sensitivities here falsely appear as detected defects. While defect 6 is detected in the pre-processed data in a large part of the measurements from test series 2, defect 5 is only detected in 3 of 35 tests (at $k = 22$ mm and $t_{\mathrm{exc}} = 30$ s, at $k = 43$ mm and $t_{\mathrm{exc}} = 20$ s, at $k = 114$ mm and $t_{\mathrm{exc}} = 15$ s), defect 7 not once. At this point, the contrast enhancement by means of PCA is an option. In Figure 7d, the effect of PCA is already visible just after the pre-processing. Defect 6 clearly stands out as a

local maximum in temperature compared to the raw image. Defect 5 is also slightly visible, while defect 7 is barely visible. The PCA-based image with filtering as well as the automatic defect detection and the calculation of the CNR in Figure 7e shows that all 3 defects are detected as such. As in the reference image without filtering, false detections occur at the edges. Due to the low contrast of defect 7, the threshold for this automatic detection had to be low as well. Changing the threshold to a higher value results in the disappearance of the falsely detected artefacts. However, a higher threshold value also leads to defect 7 not being detected by the algorithm even though it is visible in the processed data to the human observer. While defect 5 and 6 have depth-to-diameter ratios of 0.69 and 0.73, respectively, and are thus within the maximum detected ratios of current research, even defect 7 is detected with a depth-to-diameter ratio of 1.04. This confirms the current view in the literature that defects with a depth-to-diameter ratio of $\geq$1 are difficult to detect.

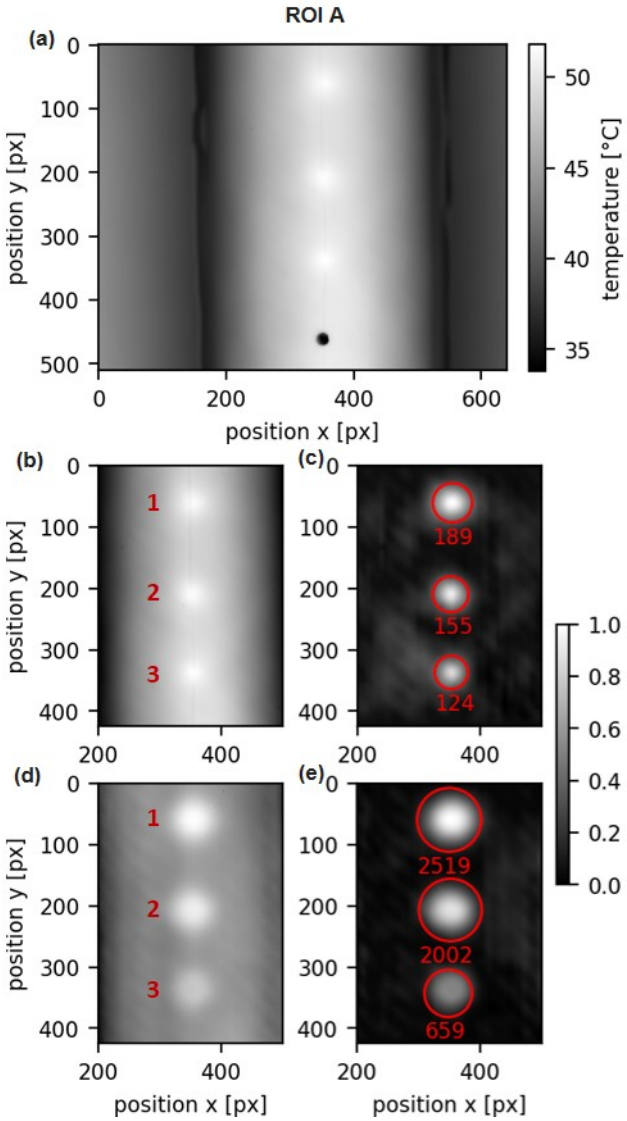

Figure 6. Results of test series 1 (ROI A, $t_{exc} = 25\,s$, $t_{rec} = 15\,s$, $k = 89\,mm$, (**a**) surface temperature of the whole camera FOV, (**b**) result for the reference method without filtering at $t_{rec} = 0\,s$, (**c**) reference image with filtering, automatic defect detection and calculation of the CNR, (**d**) result for the PCA-based method without filtering, (**e**) PCA-based image with filtering, automatic defect detection and calculation of the CNR.

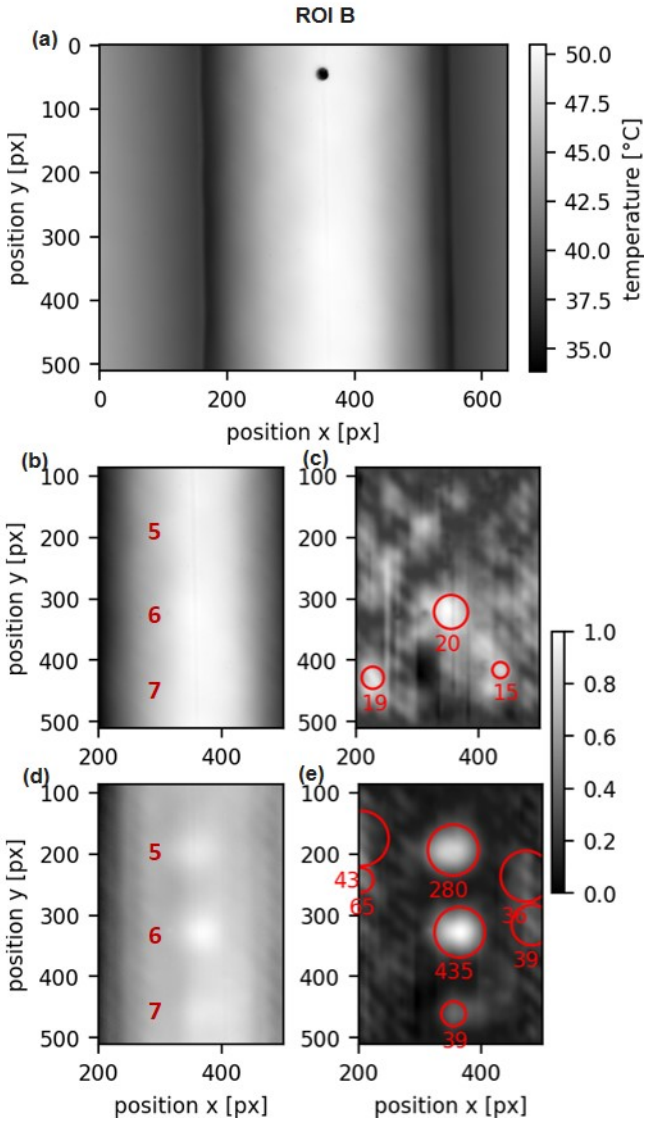

Figure 7. Results of test series 2 (ROI B, $t_{exc} = 25\,s$, $t_{rec} = 15\,s$, $k = 89\,mm$, (**a**) surface temperature of the whole camera FOV, (**b**) result for the reference method without filtering at $t_{rec} = 0\,s$, (**c**) reference image with filtering, automatic defect detection and calculation of the CNR, (**d**) result for the PCA-based method without filtering, (**e**) PCA-based image with filtering, automatic defect detection and calculation of the CNR.

In the results from test series 2, it should be noted that defect 6 stands out significantly more from its environment than defect 5, although defect 6 has a smaller diameter and a higher depth-to-diameter ratio, which means that the defect should be less visible according to the considerations from test series 1. The reason for this must therefore be the depth at which the defects are located. Defect 6 at 2.2 mm depth is closer to the surface than defect 5 at the depth 2.4 mm. While the difference between the two defects in depth is only 0.2 mm, the difference in diameter is 0.5 mm. It can be concluded from this that the distance between the surface and the defect has to be more important than the defect diameter in the detection of defects by thermography, besides the overall relationship between defect depth, thermal transfer time and observation period. A possible explanation is found in the thermal properties of GFRP. Since it is an anisotropic material, the thermal conductivity is directionally dependent [34]. Here, the heat preferentially propagates in the fiber direction, especially within one layer. The thermal conductivity perpendicular to the stacking of the layer is weaker because of the low thermal conductivity of the epoxy resin used to connect the single layers. In order to detect the thermal effects of the defect at the surface, the heat

must propagate perpendicular to the fiber direction. Propagation perpendicular to the fiber direction happens more slowly than propagation lateral to the surface. Therefore, the heat is dissipated laterally more prominently than it can dissipate to the surface, thus making surface temperature differences less pronounced or even insignificant. In case of CFRP, these thermal effects are more pronounced, since the thermal conductivity depends even more on the actual fiber direction [17]. In isotropic materials such as steel, there is no directional dependence of the thermal conductivity [35].

The investigations have shown that sub-surface defects located in a coated test specimen that closely emulates the real rotor blade leading edge can be detected by means of long-pulse thermography with a depth-to-diameter ratio of up to 1.04. Here, the detectability of the defect depends mainly on the defect depth in addition to the defect diameter. False detections occur mainly due to the inhomogeneous material. When it comes to the application of the measurement method to a rotor blade leading edge in situ, it is probably difficult to distinguish between an actual defect and a material inhomogeneity such as a resin accumulation on the basis of the thermogram, since the location of a defect on the rotor blade is unknown. How this can be dealt with will have to be shown when the measurement method is actually tested in the open field.

4.2. Influence of the Excitation Time on Sub-Surface Defect Detectability

In test series 1 and 2, both different excitation times and different distances between the excitation unit and the test specimen were investigated. However, changing the distance k, which modulates the energy introduction into the test specimen, proved to be impractical especially in the in situ application. Therefore, the focus is now on the investigations with varied excitation time since this can be easily implemented in the open field as well. Figure 8 shows the CNR values of all investigations from test series 1 and 2 at different excitation times. For the diagram, the CNR values of each detected defect at the corresponding excitation time are arithmetically averaged over all investigated distances to obtain a tendency for the behaviour of the CNR. Figure 8a shows the evolution of the mean CNR values of the reference data with filtering, averaged over the distances k at different excitation times. Defects 1 to 3 are detected in the reference data with filtering, while defects 5 to 7, which are located deeper below the surface, remain hidden. The averaged CNR of all defects ranges from 101 to 210, with a tendency to show a maximum CNR value at an excitation time interval of $t_{\mathrm{exc}} = [15 \ldots 25]$ s. The existence of such a maximum shows that there is an optimal excitation time for each depth at which a defect is located.With a short excitation time, the defect stands out less from its surroundings or is not detectable at all, because the heat in the material flowing back to the surface may be too small to provide a local temperature change at the surface of the measurement object. With a longer excitation time, on the other hand, the surrounding area of the defect is also heated to such an extent that the defect is less likely to stand out from its surroundings during the cooling phase. The diameter of a defect has no direct influence on the optimum excitation duration for a given depth. In this case (i.e., at a constant depth), it only affects the contrast of the individual defect.

Figure 8b shows the averaged CNR values of the pre-processed image, including the error bars as a measure of the scatter. The CNR values of the detected defects 1 to 3 are significantly higher than for the raw data. In particular, the visibility of the defects 1 and 2 is significantly increased by the application of PCA. Thus, the CNR values are between 940 and 1861, which corresponds to a factor of about 9 compared to the reference data with filtering for these two defects. The tendency from the reference data with filtering for a maximum CNR to occur at an excitation time interval of $t_{\mathrm{exc}} = [15 \ldots 25]$ s is clearly seen for defects located about 1.5 mm below the surface. Defect 3, on the other hand, shows a less pronounced increase in CNR (around a factor of 3) and has the maximum CNR already at an excitation duration of 20 s. This phenomenon is not observable on the basis of the raw data. However, both too short and too long excitation durations lead to lower CNR values, which is consistent with the previous results. The CNR values for the defects 5 and

6 range between 111 and 306, but so far do not show any discernible maximum in the parameters investigated. Since defect 5 and 6 are significantly located further from the surface than defects 1 to 3, and the depth has a significant influence on the defect visibility, an optimal excitation time for the corresponding depth of approx. 2.5 mm might occur outside the excitation times investigated. Panella et al. [15] obtained an optimum excitation time of 25 s in their investigations on a flat GFRP plate, but for different depths. Therefore, the extent to which the optical excitation time depends on the depth of a defect requires further investigation.

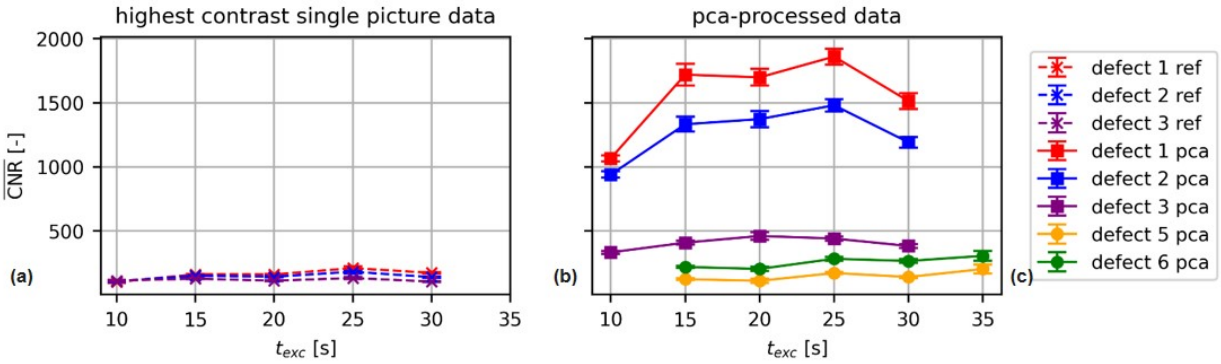

Figure 8. Mean CNR averaged over distance k at different t_{exc} of the defects 1 to 6 with error bars representing the standard deviation of the averaged CNR value, (**a**) reference data with filtering (ref)—note: defect 5 and 6 could not be detected, (**b**) PCA-based data with filtering (PCA), (**c**) legend.

The studies show that for defects of different depths, there are corresponding intervals of excitation time at which the detectability of the defect is optimal. Here, the deeper the defect is located below the surface, the longer the excitation time is required for optimum detectability. When inspecting the rotor blade leading edge in situ, it must first be clarified to what depth defects need to be detected. This determines whether one excitation duration is sufficient for inspection, or whether the leading edge must be inspected twice, each time with different excitation durations.

4.3. Influence of the Angular Perspective on Sub-Surface Defect Detectability

An essential characteristic of a rotor blade leading edge is its strong curvature. In reality, defects such as air inclusions do not always occur directly at the front of the leading edge, but also to the left or right of it. In addition, while inspecting a rotor blade leading edge, the interlocked thermographic system consisting of the infrared camera and the excitation unit may not always be aligned perpendicular to the surface. To investigate this case, the test specimen in test series 3 was rotated by the angle $\alpha = 25°$ as well as by the angle $\beta = 45°$ to the optical axis of the thermographic system at an excitation time of $t_{exc} = 25$ s; see Figure 4. The results of this investigation are shown in Figures 9 and 10.

Figure 9 shows the examination of the test specimen at an angle of $\alpha = 25°$. As in the test series before, the defects are already visible after the pre-processing (Figure 9b,d). The filtering increases the contrast, and all three defects are successfully detected (Figure 9c,e). However, here, the CNR is smaller compared to the images where the camera is oriented head-on to the defect area. Furthermore, since the excitation is rotated 25° to the defect area, it is heated less and the CNR decreases. Despite the lower CNR and the high depth-to-diameter ratio of 0.75 of defect 3, it is still successfully detected. The same trend continues in the images taken at an angle of $\beta = 45°$; see Figure 10. Again, the CNR decreases because of the increased angle between the defects, the excitation and the camera. Even in this test scenario, defect 3 is still successfully detected.

To conclude, defects that do not lie in the optical axis of the camera due to the curvature of a target can still be detected, but they stand out from their surroundings with a lower intensity than the defects that have a smaller or no angular deviation from the optical axis

of the camera. For the application at the leading edge of the rotor blade, this means that the measuring system does not have to be aligned head-on to the leading edge if this is not possible. Defects located slightly off-center of the image area at a curve can still be detected as long as the area is heated adequately and the depth of field of the camera is sufficient.

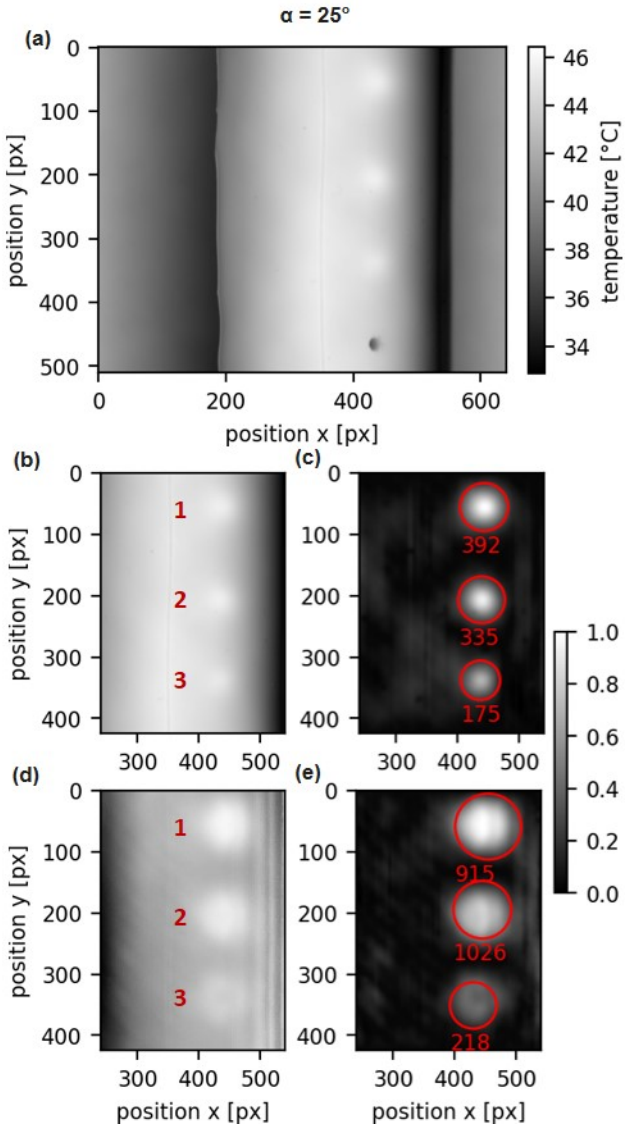

Figure 9. Results of test series 3 ($\alpha = 25°$, ROI A, $t_{exc} = 25\,s$, $t_{rec} = 15\,s$, $k = 89\,mm$, (**a**) surface temperature of the whole camera FOV, (**b**) result for the reference method without filtering at $t_{rec} = 0\,s$, (**c**) reference image with filtering, automatic defect detection and calculation of the CNR, (**d**) result for the PCA-based method without filtering, (**e**) PCA-based image with filtering, automatic defect detection and calculation of the CNR.

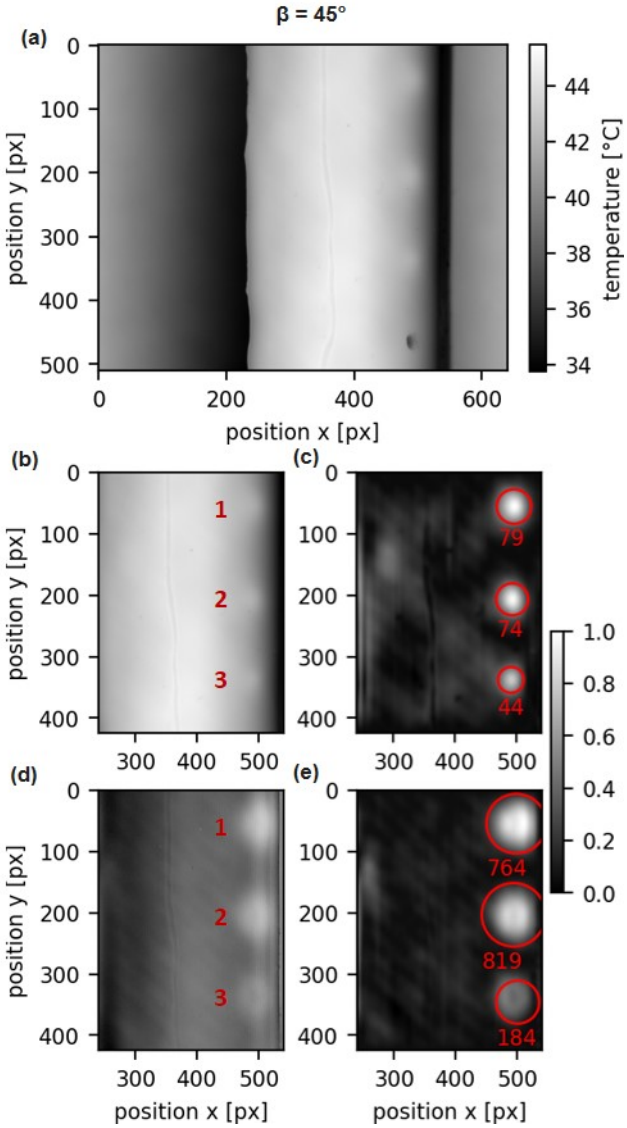

Figure 10. Results of test series 3 ($\beta = 45°$, ROI A, $t_{exc} = 25\,s$, $t_{rec} = 15\,s$, $k = 89\,mm$, (**a**) surface temperature of the whole camera FOV, (**b**) result for the reference method without filtering at $t_{rec} = 0\,s$, (**c**) reference image with filtering, automatic defect detection and calculation of the CNR, (**d**) result for the PCA-based method without filtering, (**e**) PCA-based image with filtering, automatic defect detection and calculation of the CNR.

5. Conclusions and Outlook

For the investigation of the rotor blade leading edge of wind turbines, long-pulse thermography was presented as a measuring method, which is suitable for the detection of initial inhomogeneities below the surface. A GFRP test specimen with a curved surface, an applied coating system and modified with different drillings served as a reference object. The structural and material design as well as the geometrical dimensions correspond to a real rotor blade leading edge, which allows for a transferability of the results to reality. To reduce side effects like inhomogeneous heating or thermal reflections in the thermographic image as well as to increase the contrast, PCA was used as the image processing method. All output images were quantified and analysed by calculating the CNR value of each detected defect. The investigations have shown that

- Sub-surface defects can also be detected on strongly curved and coated test specimens, which are similar in size and structural design to the leading edge of a rotor blade in the tip area.

- Sub-surface defects with a depth-to-diameter ratio of up to 1.04 were detected, which exceeds the previously detected depth-to-diameter ratios of up to 0.825 on flat plates.
- The determined CNR value depends significantly on the depth at which a defect is located rather than the diameter of the defect.
- Sub-surface defects that have an angular offset from the optical axis of the camera and are therefore subject to the object's curvature can also be detected, but with a decreasing CNR value as the viewing angle increases.
- There is an optimal excitation time depending on the depth of a defect: For a defect with a depth of 1.5 mm, an excitation time of 15 s to 25 s was found to be optimal. For defects at a depth of 2.5 mm, no optimal excitation duration could be determined based on the available experimental data.

For a complete examination of the leading edge, the effects of different surface curvatures, eccentric inhomogeneities as well as typical defects like voids in the coating system or delaminations in the GFRP should additionally be examined regarding their detectability. In addition, modified test specimens will be exposed to rain loading to observe the damage evolution of the sub-surface defects and provide a prediction for the size as well as the timing of the occurrence of a surface defect. For further investigations concerning an optimal excitation duration as a function of the defect depth, it is therefore recommended to perform parameter studies by means of experiments and simulations. In addition, it is recommended to apply other evaluation methods in addition to PCA, such as pattern and edge detection, to provide defect detection suitable for on-site applications. Finally, investigations in the open field at the rotor blade leading edge of a real wind turbine are to be carried out to validate the in situ capability of the proposed measurement method.

Author Contributions: Conceptualization, F.J., M.S. and A.F.; methodology, F.J.; software, F.J. and M.T.; validation, F.J. and M.T.; formal analysis, F.J.; investigation, F.J. and M.T.; resources, F.J., M.S. and A.F.; data curation, F.J. and M.T.; writing—original draft preparation, F.J.; writing—review and editing, M.S. and A.F.; visualization, F.J. and M.T.; supervision, M.S. and A.F.; project administration, F.J.; funding acquisition, M.S. All authors have read and agreed to the published version of the manuscript.

Funding: This research was funded by the Bundesministerium für Wirtschaft und Energie (BMWI), grant number 20794 N/2 and the Arbeitsgemeinschaft industrieller Forschung (AIF).

Institutional Review Board Statement: Not applicable.

Informed Consent Statement: Not applicable.

Acknowledgments: The authors would like to thank the Fraunhofer IFAM, the companies of 3M and AkzoNobel for the preparation of the test specimens used in this work. Furthermore, we would like to thank the company InfraTec for their advice and support during the thermographic measurements.

Conflicts of Interest: The authors declare no conflict of interest.

Nomenclature

The following nomenclature is used in this manuscript:

CFRP	carbon fiber-reinforced plastic
CNR	contrast-to-noise ratio
GFRP	glass fiber-reinforced plastic
PCA	principal component analysis
ROI	region of interest
SNR	signal-to-noise ratio
A	normalized matrix
$C_{a,A-B}$	absolute contrast between area A and B
d_j	defect diameter in [mm]
h_j	defect depth in [mm]
$\hat{I}_A$, $\hat{I}_B$	mean intensity of area A, B
k_j	distance between excitation unit and test sample in [mm]

r_i	inner radius in [mm]
s	wall thickness in [mm]
s_{GFRP}	wall thickness of GFRP half pipe in [mm]
S	singular value matrix
S_A, S_B	standard deviation of area A, B
S_{A-B}	standard deviation of area A and B
U	matrix of empirical orthogonal functions
t_{exc}	excitation time in [s]
t_{rec}	recording time in [s]
V^T	transposed matrix with principal components
α, β	angle in [○]

References

1. Sagol, E.; Reggio, M.; Ilinca, A. Issues concerning roughness on wind turbine blades. *Renew. Sustain. Energy Rev.* **2013**, *23*, 514–525. [CrossRef]
2. Gaudern, N. A practical study of the aerodynamic impact of wind turbine blade leading edge erosion. *J. Phys. Conf. Ser.* **2014**, *524*, 012031. [CrossRef]
3. Timmer, W.A.; Schaffarczyk, A.P. The effect of roughness at high Reynolds numbers on the performance of aerofoil DU 97-W-300Mod. *Wind Energy* **2004**, *7*, 295–307. [CrossRef]
4. Dollinger, C.; Balaresque, N.; Gaudern, N.; Sorg, M.; Fischer, A. Calculation of the power output loss based on thermographic measurement of the leading edge condition. *J. Phys. Conf. Ser.* **2018**, *1037*, 052011. [CrossRef]
5. Herring, R.; Dyer, K.; Martin, F.; Ward, C. The increasing importance of leading edge erosion and a review of existing protection solutions. *Renew. Sustain. Energy Rev.* **2019**, *115*, 109382. [CrossRef]
6. Keegan, M.H. Wind Turbine Blade Leading Edge Erosion: An Investigation of Rain Droplet and Hailstone Impact Induced Damage Mechanisms. Ph.D. Thesis, University of Strathclyde, Glascow, UK, 2014.
7. Schmitt, G.F., Jr. *Materials Paramteres that Govern the Rain Erosion Behavior of Polymeric Coatings and Composites at Subsonic Velocities*; Air Force Materials Laboratory Wright-Patterson AFB: Greene County, OH, USA, 1971.
8. Zhang, S.; Dam-Johansen, K.; Nørkjær, S.; Bernad, P.L.; Kiil, S. Erosion of wind turbine blade coatings—Design and analysis of jet-based laboratory equipment for performance evaluation. *Prog. Org. Coat.* **2015**, *78*, 103–115. [CrossRef]
9. Beganovic, N.; Söffker, D. Structural health management utilization for lifetime prognosis and advanced control strategy deployment of wind turbines: An overview and outlook concerning actual methods, tools, and obtained results. *Renew. Sustain. Energy Rev.* **2016**, *64*, 68–83. [CrossRef]
10. Yang, R.; He, Y.; Zhang, H. Progress and trends in nondestructive testing and evaluation for wind turbine composite blade. *Renew. Sustain. Energy Rev.* **2016**, *60*, 1225–1250. [CrossRef]
11. Du, Y.; Zhou, S.; Jing, X.; Peng, Y.; Wu, H.; Kwok, N. Damage detection techniques for wind turbine blades: A review. *Mech. Syst. Signal Process.* **2020**, *141*, 106445. [CrossRef]
12. Meinlschmidt, P.; Aderhold, J. Thermographic Inspection of Rotor Blades. In Proceedings of the 9th European Conference on NDT, Berlin, Germany, 25–29 September 2006.
13. Almond, D.P.; Angioni, S.L.; Pickering, S.G. Long pulse excitation thermographic non-destructive evaluation. *NDT E Int.* **2017**, *87*, 7–14. [CrossRef]
14. Lizaranzu, M.; Lario, A.; Chiminelli, A.; Amenabar, I. Non-destructive testing of composite materials by means of active thermography-based tools. *Infrared Phys. Technol.* **2015**, *71*, 113–120. [CrossRef]
15. Panella, F.W.; Pirinu, A.; Dattoma, V. A Brief Review and Advances of Thermographic Image-Processing Methods for IRT Inspection: A Case of Study on GFRP Plate. *Exp. Tech.* **2020**, *45*, 429–443. [CrossRef]
16. Wei, Y.; Su, Z.; Mao, S.; Zhang, D. An Infrared Defect Sizing Method Based on Enhanced Phase Images. *Sensors* **2020**, *20*, 3626. [CrossRef] [PubMed]
17. Maierhofer, C.; Röllig, M.; Gower, M.; Lodeiro, M.; Baker, G.; Monte, C.; Adibekyan, A.; Gutschwager, B.; Knazowicka, L.; Blahut, A. Evaluation of Different Techniques of Active Thermography for Quantification of Artificial Defects in Fiber-Reinforced Composites Using Thermal and Phase Contrast Data Analysis. *Int. J. Thermophys.* **2018**, *39*. [CrossRef]
18. Wang, Z.; Tian, G.; Meo, M.; Ciampa, F. Image processing based quantitative damage evaluation in composites with long pulse thermography. *NDT E Int.* **2018**, *99*, 93–104. [CrossRef]
19. Kamińska, P.; Ziemkiewcz, J.; Synaszko, P.; Dragan, K. Comparison of Pulse Thermography (PT) and Step Heating (SH) Thermography in Non-Destructive Testing of Unidirectional GFRP Composites. *Fatigue Aircr. Struct.* **2019**, *2019*, 87–102. [CrossRef]
20. Almond, D.P.; Angioni, S.L.; Pickering, S.G. Thermographic NDE advisory and guidance system. *NDT E Int.* **2016**, *83*, 134–142. [CrossRef]
21. Wei, Z.; Fernandes, H.; Herrmann, H.G.; Tarpani, J.R.; Osman, A. A Deep Learning Method for the Impact Damage Segmentation of Curve-Shaped CFRP Specimens Inspected by Infrared Thermography. *Sensors* **2021**, *21*, 395. [CrossRef]

22. Da Silva, W.F.; Melo, R.A.C.; Grosso, M.; Pereira, G.R.; Riffel, D.B. Active Thermography Data-Processing Algorithm for Nondestructive Testing of Materials. *IEEE Access* **2020**, *8*, 175054–175062. [CrossRef]
23. Pastuszak, P.D. Characterization of Defects in Curved Composite Structures Using Active Infrared Thermography. *Procedia Eng.* **2016**, *157*, 325–332. [CrossRef]
24. Ibarra-Castanedo, C.; Avdelidis, N.P.; Grenier, M.; Maldague, X.; Bendada, A. Active thermography signal processing techniques for defect detection and characterization on composite materials. In *Thermosense XXXII*; Dinwiddie, R.B., Safai, M., Eds.; International Society for Optics and Photonics: Orlando, FL, USA, 2010; Volume 7661, p. 76610O. [CrossRef]
25. Roche, J.M.; Leroy, F.H.; Balageas, D.L. Images of TSR coefficients: A sinple way for a rapid and efficient detectin of defects. *Mater. Eval.* **2013**, *72*, 73–82.
26. Lopez, F.; Maldague, X.; Ibarra-Castanedo, C. Enhanced image processing for infrared non-destructive testing. *Opto-Electron. Rev.* **2014**, *22*. [CrossRef]
27. Sanati, H.; Wood, D.; Sun, Q. Condition Monitoring of Wind Turbine Blades Using Active and Passive Thermography. *Appl. Sci.* **2018**, *8*, 2004. [CrossRef]
28. Rodriguez-Molares, A.; Rindal, O.M.H.; D'hooge, J.; Masoy, S.E.; Austeng, A.; Lediju Bell, M.A.; Torp, H. The Generalized Contrast-to-Noise Ratio: A Formal Definition for Lesion Detectability. *IEEE Trans. Ultrason. Ferroelectr. Freq. Control* **2020**, *67*, 745–759. [CrossRef] [PubMed]
29. Dollinger, C. Thermografische Strömungsvisualisierung an Rotorblättern von Windenergieanlagen. Ph.D. Thesis, Universität Bremen, Bremen, Germany, 2018.
30. Rajic, N. *Principal Component Thermography*; DSTO. Aeronautical and Maritime Research Laboratory: Fisherman's Bend, Australia, 2002.
31. Rajic, N. Principal component thermography for flaw contrast enhancement and flaw depth characterisation in composite structures. *Compos. Struct.* **2002**, *58*, 521–528. [CrossRef]
32. Hau, E. *Windkraftanlagen: Grundlagen, Technik, Einsatz, Wirschaftlichkeit*, 5th ed.; Springer: Berlin/Heidelberg, Germany, 2014. [CrossRef]
33. Abbott, I.H.; Dodenhof, A.E.; Stivers, L.S., Jr. *NACA TR 824—Summary of Airfoil Data*; National Advisory Committee for Aeronautics: Washington, DC, USA, 1945.
34. Schürmann, H. *Konstruieren mit Faser-Kunststoff-Verbunden*, 2nd ed.; Spinger: Berlin/Heidelberg, Germany, 2007.
35. Arora, V.; Mulaveesala, R.; Dua, G.; Sharma, A. Thermal non-destructive testing and evaluation for subsurface slag detection: Numerical modelling. *Insight Non-Destr. Test. Cond. Monit.* **2020**, *62*, 264–268. [CrossRef]